



ELSEVIER

Contents lists available at ScienceDirect

Journal of Theoretical Biology

journal homepage: www.elsevier.com/locate/yjtbi

Holotestoid: A computational model for testing hypotheses about echinoid skeleton form and growth

Maria Abou Chakra^a, Jonathon Richard Stone^{b,*}

^a McMaster University, Department of Biology, 1280 Main Street West, Hamilton, ON, Canada L8S 4K1

^b McMaster University, Department of Biology and Origins Institute, 1280 Main Street West, Hamilton, ON, Canada L8S 4K1

ARTICLE INFO

Article history:

Received 28 May 2010

Received in revised form

10 June 2011

Accepted 17 June 2011

Available online 2 July 2011

Keywords:

Bubbles

Close-packing

Growth zone

Plate patterns

Theoretical morphology graphic simulation

ABSTRACT

Regular echinoid skeletons, or tests, comprise plate patterns and overall shapes that have proven challenging to analyse solely on the basis of any one approach or process. Herein, we present a computational model, Holotestoid, that emulates four macrostructural ontogenic processes involved in test growth (plate growth, plate addition, plate interaction, and plate gapping). We devise a geometric representation for analysing tests and describe how we use analogies (bubble interactions and close-packing) to emulate the processes. In the computational model, the emulated processes are used to determine the plate size and plate shape and combined to simulate a growth zone. We simulated growth zones for *Arbacia punctulata* and for *Strongylocentrotus franciscanus* by changing the value for one parameter, the ambulacral column angle. We quantitatively compared morphological features for simulated forms to those for real specimens to test the computational model. Additionally, we simulated growth zones for *A. punctulata*, *S. franciscanus*, *Euclidaris thoursii*, and *Mellita quinquesperforata* by changing three parameters, ambulacral column angle, peristome radius to apical system radius ratio, and apical system radius to column length ratio. Holotestoid can be used to explain morphological disparity among echinoid tests.

© 2011 Elsevier Ltd. All rights reserved.

1. Introduction

Echinoid skeletons, or tests, are classified as permanent and mutable endoskeletons; skeletal form within an individual is retained, with changes occurring through growth (Vermeij, 1970). Echinoids present ideal systems for studying diminishing or regenerating calcified structures (Märkel and Roser, 1983). Knowledge about echinoid test growth can be implemented toward understanding vertebrate skeletons, as they also are permanent and mutable endoskeletons. However, describing and explaining echinoid test growth has proven challenging for researchers because factors such as individual longevity (*i.e.*, an over 100-year life span; Ebert and Southon, 2003) and internalisation prohibiting direct access (Hyman, 1955) have hindered analysis. Herein, we present Holotestoid, a computational model designed to explore regular echinoid test growth in a manner that cannot be analysed practically through *in vivo* experimental techniques. Holotestoid provides a tool for describing and explaining the morphological disparity that is observed among echinoid tests (Jackson, 1912; Kier, 1974; Smith, 2005).

1.1. Echinoid form

Echinoid tests comprise microstructures and macrostructures. Microstructurally, the plates within tests involve three-dimensional meshworks, mineralised trabeculae containing magnesium calcite with minor additions of protein in minor associations, termed stereom (Märkel and Roser, 1985). Pores among trabeculae are suited ideally for fibrous tissue such as fibrocytes, sclerocytes, and collagen to be inserted. Collagen fibres suture adjacent plates together, but they also provide flexibility to tests (Ellers *et al.*, 1998; Johnson *et al.*, 2002).

Macrostructurally, plates, themselves, function as the 'building blocks' in echinoid tests. Five different plate types define three distinct regions (Fig. 1). The peristome (*ps*) contains buccal plates (Fig. 1) and, in some species, primordial ambulacral plates (Hyman, 1955); the apical system (*ap*) contains genital (*ge*) plates and ocular (*oc*) plates; and the corona (*cr*) contains ambulacral (*am*) plates and interambulacral (*ia*) plates (Fig. 1). Plate arrangements within these regions produce pentamerous symmetry, an echinoderm characteristic (Hyman, 1955).

Each echinoid test is divided into five growth zones. A growth zone (*gz*) is a section containing biserial ambulacral columns and two flanking interambulacral columns. All plates within a growth zone nucleate from the same ocular plate (Jackson, 1912; Mooi *et al.*, 1994; Mooi and David, 1996).

* Corresponding author. Tel.: +1 905 525 9140x26136, lab: +1 905 525 9140x27676; fax: +1 905 522 6066.

E-mail addresses: abouchm@mcmaster.ca (M. Abou Chakra), jstoner@mcmaster.ca (J.R. Stone).

Nomenclature

<i>ab</i>	ambitus
<i>am</i>	ambulacral plates
<i>ap</i>	apical system
<i>cl</i>	column length
<i>cr</i>	corona
<i>d_p</i>	distance from the polar region to a plate
<i>ge</i>	genital plates
<i>gz</i>	growth zone
<i>ia</i>	interambulacral plates
<i>oc</i>	ocular plates
<i>oh</i>	ocular plate height
<i>ow</i>	ocular plate width
<i>ps</i>	peristome
<i>ph</i>	interambulacral plate height

<i>pw</i>	interambulacral plate width
<i>r_X</i>	radius for bubble or circle <i>X</i> , with <i>X</i> =A, B, C, D in different parts in the text
<i>S_{plate}</i>	plate size (diameter for circle representing plate)
<i>α</i>	column angle (general)
<i>α_{ia}</i>	interambulacral column angle
<i>α_{Nam}</i>	new ambulacral plate nucleation angle
<i>α_{Nia}</i>	new interambulacral plate nucleation angle
<i>α_{Npia}</i>	interambulacral plate angle
<i>t_{pn}</i>	total plate number
<i>α_{gz}</i>	growth zone angle
<i>α_{am}</i>	ambulacral column angle
<i>ap_r</i>	apical system radius
<i>ps_r:ap_r</i>	peristome radius to apical system radius ratio
<i>ap_r:cl</i>	apical system radius to column length

1.2. Echinoid growth

We limit our echinoid test growth description to the macrostructural level. Plate ontogeny plays a major role in test growth, through five macrostructural ontogenic processes. Four processes are direct – plate growth, plate addition, plate interaction, plate gapping, and one is indirect – visceral growth. Plate growth is the process by which calcite accretes or resorbs peripherally (Pearse and Pearse, 1975; Märkel, 1981). Plate addition is the process whereby plates are added contiguous with ocular plates (Jackson, 1912; Mooi et al., 1994; Mooi and David, 1996). Plate interaction is the process by which plates touch and interconnect directly or indirectly with each other (Moss and Meehan, 1967; Raup, 1968). Plate gapping is the process whereby collagen fibres loosen, allowing plates to separate from one another (Ellers et al., 1998; Johnson et al., 2002). Visceral growth is the process wherein effects imparted by somatic growth onto skeletal structures are integrated (Deutler, 1926; Gordon, 1926; Ellers and Telford, 1992). These five processes are interrelated and occur simultaneously. Consequently, empirically differentiating the direct contribution by each individual process to ontogeny is challenging. Thus, researchers have adopted theoretical modelling as an alternative technique suited for elucidating echinoid test growth.

1.3. Theoretical models

Within the past century, nine theoretical models have been proposed to describe or explain growth in extant regular echinoid tests (Thompson, 1917; Moss and Meehan, 1968; Raup, 1968; Seilacher, 1979; Telford, 1985, 1994; Baron, 1990, 1991; Ellers, 1993; Zachos, 2009; Abou Chakra and Stone, 2008; reviewed in Abou Chakra and Stone, 2011). At least one macrostructural ontogenic process was excluded from each model (in the following descriptions, we present the models specifically as they relate to the five processes). Three models include one process: Thompson (1917) considered visceral growth, using liquid drops as an analogy to describe test form; Moss and Meehan (1968) considered visceral growth, likening regular test growth to mammalian cranial expansion; and Ellers (1993) emulated visceral growth, using a liquid drop analogy and thin shell theory to explain the overall test curvature (we use the word ‘emulate’ to refer to processes and ‘simulate’ to refer to their product). Four models include two processes: Seilacher (1979) considered visceral growth, describing tests as mineralised *pneu* structures that grow when internal pressures exceed external surface tensions, and proposed that diverse morphologies result from differential plate growth gradients; Telford (1985, 1994) described

plate addition and plate growth, hypothesising that tests are constructed to resist external forces and using the mechanics associated with dome structures as an analogy to explain structural strength; Baron (1990, 1991) created a computational model in which plate growth was determined by ‘hoop’ growth equations, which, themselves, were determined from finite-element analysis, and visceral growth, which was regulated on the basis of height-to-diameter ratios and internal pressure; and Zachos (2009) computationally described visceral growth, utilising Ellers’ model, and plate growth, by projecting Voronoi diagrams onto spherical surfaces. One model includes three processes: Raup (1968) emulated plate interactions, using a computational model, and described plate addition, using a logistic equation, and plate growth, using a parabolic function.

We describe herein a computational model that emulates the four direct, macrostructural ontogenetic processes. We build on Abou Chakra and Stone (2008), in which we used a bubble analogy to emulate interambulacral plate interactions as a conceptual basis for modelling echinoid tests (Thompson, 1917; Raup, 1968). That model involved a parabolic function and a logistic equation to describe plate growth and plate addition (Raup, 1968) and introduced conceptually circle-packing principles to emulate plate gapping.

We implement a geometric representation to explain plate growth and plate addition, eliminating the need for a parabolic function and logistic equation. We use physical and mathematical principles to emulate plate interactions and a novel circle-packing algorithm to emulate plate gapping. By integrating the four direct macrostructural ontogenic processes in Holotestoid, we provide researchers with a tool for gaining insight into how echinoid test morphologies are produced and have evolved.

2. Methodology

2.1. Empirical methods

We obtained live specimens of *Arbacia punctulata* ($n=33$) from Gulf Specimen Marine Laboratory, Panacea, FL, USA; *Strongylocentrotus droebachiensis* ($n=1$) and *S. franciscanus* ($n=14$) from Westwind Sealab Supplies, Victoria, BC, Canada; and *Mellita quinquesperforata* ($n=10$) from Marine Biological Laboratory, Woods Hole, MA, USA. We obtained dry test specimens of *Eucidaris thouarsii* ($n=6$) from the California Academy of Sciences collection, San Francisco, CA, USA. Sample sizes were determined by availability. Specimens of *A. punctulata* and *S. franciscanus* were used in validating the computational model (i.e., assessing whether the computational model produced morphometric variables that were

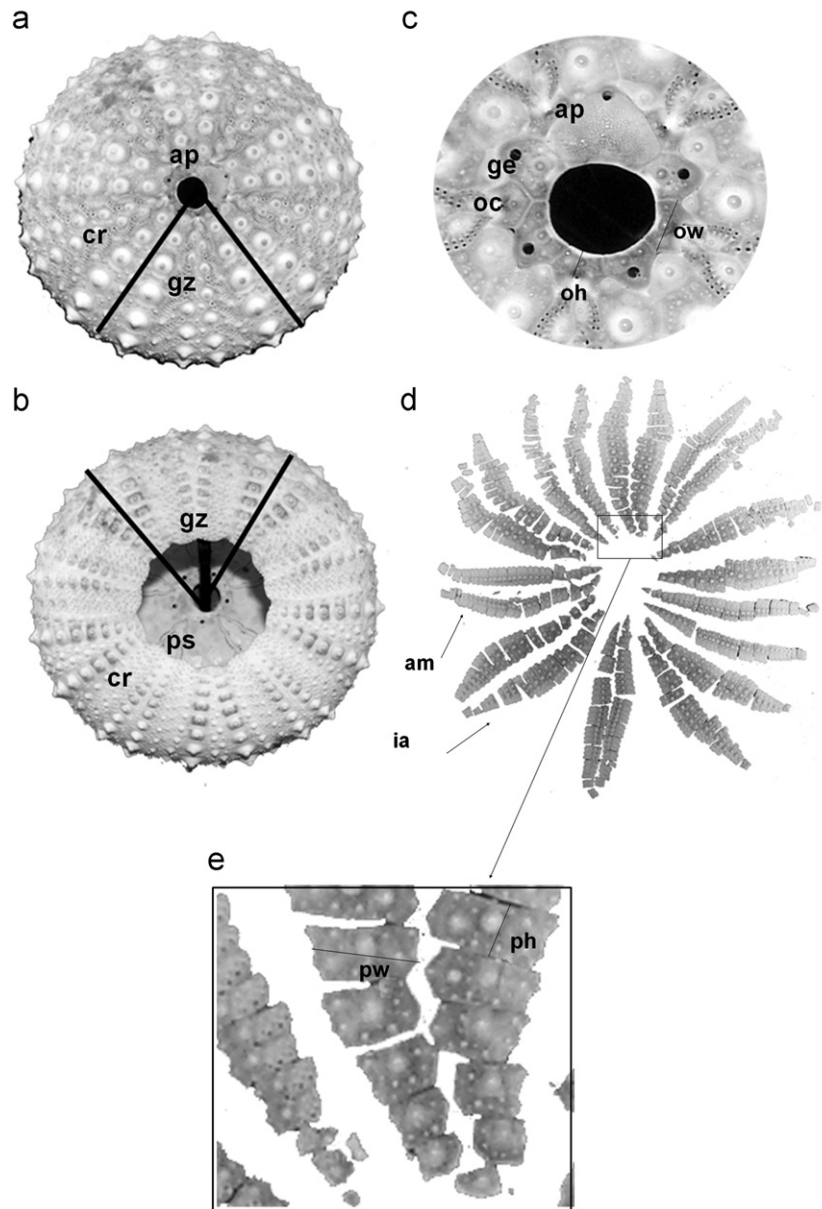


Fig. 1. Echinoid test specimens, *Strongylocentrotus fransiscanus* (a–c) and *S. droebachiensis* (d,e). (a) Apical surface, containing the apical system (*ap*), with corona (*cr*) and growth zone (*gz*); (b) oral surface, containing the peristome (*ps*); (c) apical system, containing genital plates (*ge*) and ocular plates (*oc*), with ocular plate height (*oh*) and ocular plate width (*ow*); (d) disarticulated test, revealing ambulacral columns (*am*) and interambulacral columns (*ia*); and (e) magnified interambulacral plate height (*ph*) and interambulacral plate width (*pw*).

similar to those measured from real specimens), and specimens of all four species were used in simulating growth zones.

We performed measurements on despined, eviscerated, and cleaned tests (Figs. 1 and 2): apical system (*ap*), peristome (*ps*), column length (measured from the apical system edge to the peristome, *cl*), growth zone width (*gz*), growth zone height (measured as the shortest distance from the apical system boundary to the ambitus, *ab*), ambulacral column width (*am*), ambulacral column height (measured as the shortest distance from the apical system centre to the ambitus), interambulacral plate height (*ph*), interambulacral plate width (*pw*), ocular plate height (*oh*), and ocular plate width (*ow*).

2.2. Theoretical method

The computational model, Holotestoid, can be run on a personal computer, using the technical computing environment

Mathematica 7.0 (Wolfram Research, Inc., 2009) as a software platform. Computer program code can be acquired from the supplementary materials deposited with the journal.

3. Holotestoid: modelling direct, macrostructural ontogenic processes

We designed Holotestoid to simulate growth zones for regular echinoid tests, using the following parameters: total plate number, growth zone angle (angle indicated by the spanning length *gz* in Fig. 2), ambulacral column angle (angle indicated by *am* in Fig. 2), apical system radius (Fig. 2), peristome radius to apical system radius ratio, and apical system radius to column length ratio (Fig. 2).

We developed a theoretical analytical framework for emulating the four direct macrostructural ontogenic processes, using

a geometric representation that transforms three-dimensional tests (Fig. 3a) into two-dimensional graphic objects (Fig. 3b). The transformation facilitates modelling: an inner circle represents the

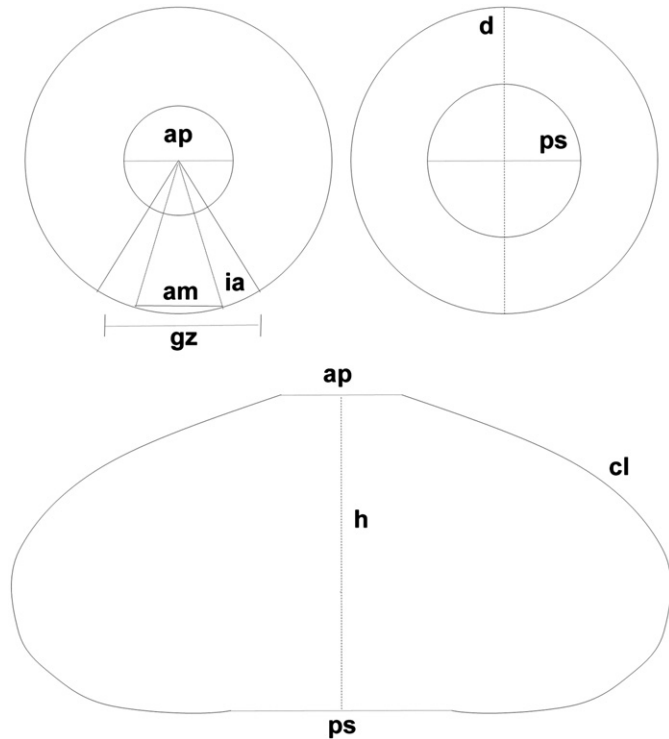


Fig. 2. Schematic representation for an echinoid test: apical system (*ap*; horizontal line represents diameter), peristome (*ps*; horizontal line represents diameter), column length (*cl*), growth zone width (*gz*), test height (*h*), ambitus diameter (*d*), ambulacral column width (*am*) and interambulacral column width (*ia*).

boundary for either an apical system (top) or peristome (bottom) and an outer circle represents a test surface with a diameter equivalent to the ambitus (Fig. 3b); circles representing the two test surfaces (aboral and oral, or upper and lower) are situated tangential to one another, thereby mimicking a continuous column (Fig. 3b). Each growth zone is divided into three sectors, distinguishing interambulacral from ambulacral columns (Fig. 3), and plates comprising columns are represented as circles (Fig. 4).

The geometric representation provides a platform to establish conceptual links among test components and to define physical features such as plate sizes, growth zone angles, and column angles. We ultimately encoded the conceptual links among test components into the computational model to emulate the four direct, macrostructural ontogenic processes. However, as insufficient information about the processes could be obtained empirically from morphological data, we first utilised analogies. For instances, the mechanisms producing curved boundaries at plate interfaces (Raup, 1968) and the distances involved in plate gapping are understood incompletely. Therefore, we used coalescing bubbles and close-packing arrangements as analogues, to describe, respectively, plate interaction and plate gapping. These analogues are understood on the basis of concrete physical principles and mathematical principles, such as Plateau's Laws, Descartes' Circle Theorem, and the Fermat Point.

3.1. Plate growth

Plate growth, plate size change, is manifested through peripheral accretion or resorption (Pearse and Pearse, 1975; Märkel and Roser, 1983). We used the geometrical representation to study the relationship between plate size and plate location. We collected interambulacral plate height (Fig. 1e) and interambulacral plate width (Fig. 1e) measurements from specimens of *A. punctulata* and *S. franciscanus*. We grouped specimens on the

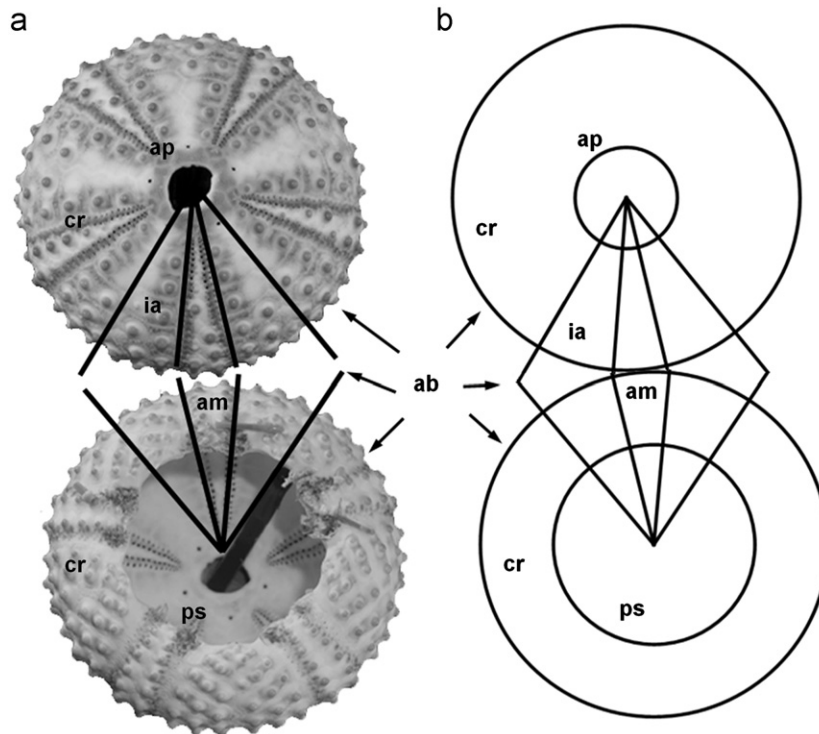


Fig. 3. Theoretical analytical framework for emulating the four direct, macrostructural ontogenic processes, using a geometric representation that transforms three-dimensional tests (a) into two-dimensional graphic objects; (a) *Arbacia punctulata* test, showing apical surface (top) and oral surface (bottom), containing apical system and peristome, respectively; (b) two-dimensional geometrical representation: inner circles represent apical system (top) and peristome (bottom) and outer circles each represent ambitus (*ab*; outer periphery for the test), to demarcate the coronal region (*cr*). (a) and (b) depict a growth zone divided into three sectors delineating ambulacral (*am*) and interambulacral (*ia*) columns.

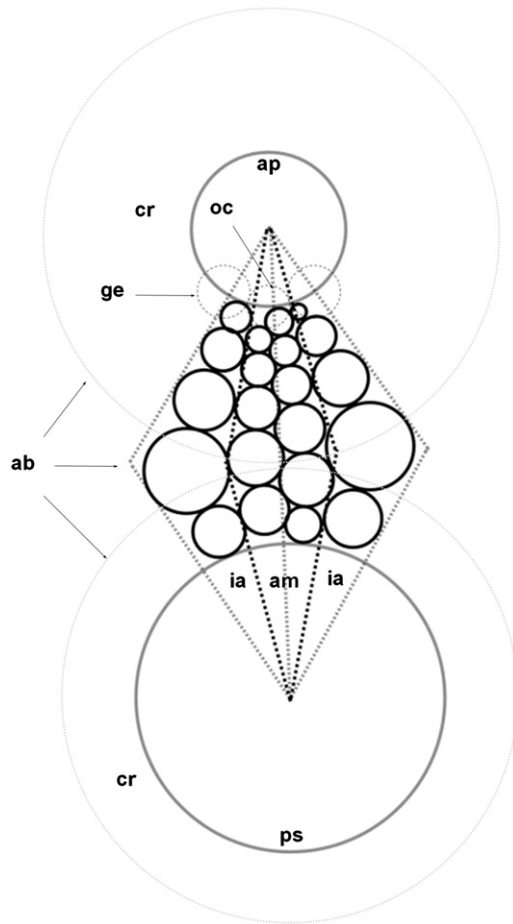


Fig. 4. Geometric representation defining test structures (regions and plates), using circles. Inner circles represent apical system (top) or peristome (bottom) and each outer, dashed circle represents an ambitus (outer periphery of the test). One growth zone is shown, with apical system (*ap*) containing genital plates (*ge*) and ocular plates (*oc*); corona (*cr*) containing ambulacral columns (*am*) and interambulacral columns (*ia*); and peristome, *ps*.

basis of plate number within each interambulacral column, which ranged from 12 to 15 for *A. punctulata* (Fig. 5a and b) and 12–20 for *S. franciscanus* (Fig. 5d and e). Plate width increased with distance from either the apical system or peristome, therefore maximising at the ambitus (peaks in Fig. 5b and e). Ambital plate height and ambital plate width increased with total plate number (Fig. 5; plates were numbered starting from the peristome and ending at the apical system). For these regular echinoid species, plate size is related to location within a growth zone, corroborating previous findings (Moss and Meehan, 1968; Raup, 1968).

We implemented the relation between plate size and plate location in the computational model. Plate size is related to relative longitudinal distance from the polar regions. Plates above the ambitus are associated with the aboral surface, containing the apical system, and plates below the ambitus are associated with the oral surface, containing the peristome (Fig. 4). Plates are ascribed as either ambulacral or interambulacral on the basis of their latitudinal position within a growth zone. Latitudinal position was determined by reference to growth zone angle (α_{gz}). Algorithmically, α_{gz} was calculated geometrically (e.g., to calculate α_{gz} , the computational model created two line segments diverging from the apical system centre and ending at the ambitus, where the linear distance between them at the ambitus was equal to the growth zone width, and rotated one line segment onto the other). Algebraically, α_{gz} is calculated as a sum between the α_{am} and the

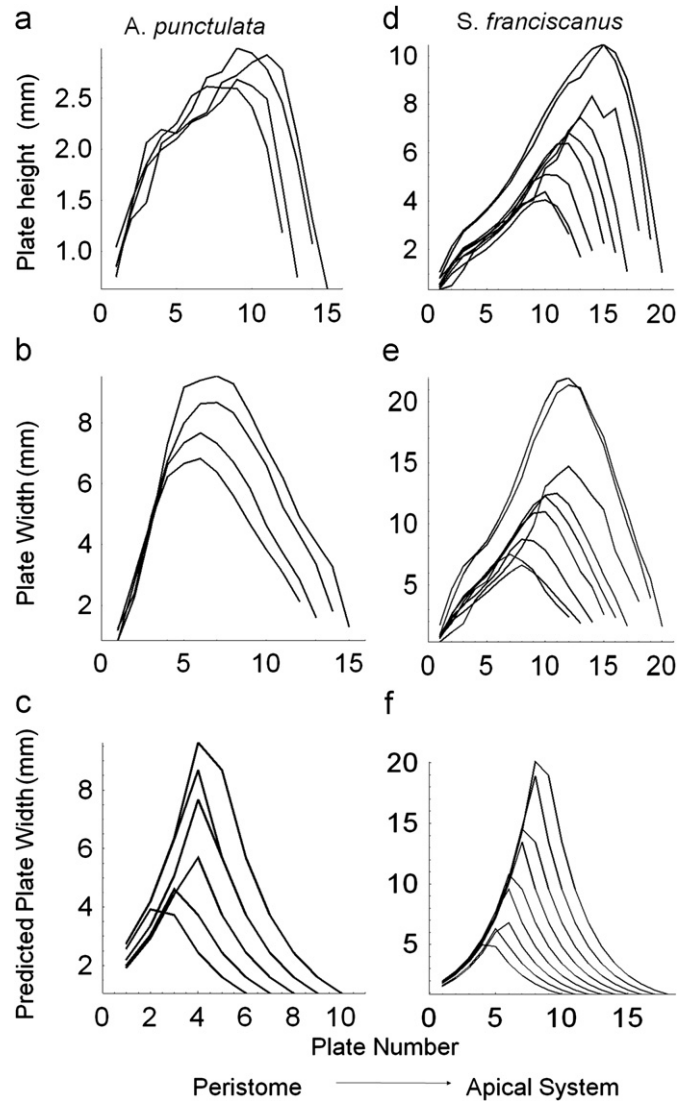


Fig. 5. Plots for (plate number, plate height) and (plate number, plate width) pairs for two sea urchin species. *A. punctulata* (a) measured plate heights from specimens containing 12–15 interambulacral plates in a column; (b) measured plate widths from specimens containing 12–15 interambulacral plates in a column; and (c) predicted plate widths from simulation representing 8–12 interambulacral plates in a column. *S. franciscanus* (d) measured plate heights from specimens containing 12–20 interambulacral plates in a column; (e) measured plate widths from specimens containing 12–20 interambulacral plates in a column; (f) predicted plate widths from simulation representing 12–18 interambulacral plates in a column (simulations involved 40 ambulacral plates, and, therefore, predicted interambulacral plate numbers differed from actual interambulacral plate numbers; plot points were joined to reveal trends and morphological features, such as the position for the ambitus).

interambulacral column angle (α_{ia}) located within it:

$$\alpha_{gz} = \alpha_{am} + \alpha_{ia} \quad (1)$$

Echinoids are characterised by pentamerous symmetry; however, for consistency, we used the geometric representation to measure growth zone sectors. Measurements from *A. punctulata* and *S. franciscanus* yielded average $\alpha_{gz} = 72 \pm 4^\circ$ and $72 \pm 3^\circ$, respectively (all \pm errors reported herein represent one standard deviation). Based on these data, we used $\alpha_{gz} = 72^\circ$ as a default. Additionally, ambulacral column angles (α_{am}) were measured with respect to the apical system for *A. punctulata* and *S. franciscanus*, yielding average $\alpha_{am} = 20 \pm 2^\circ$ and $31 \pm 3^\circ$, respectively. The measurements show that α_{am} values can distinguish empirically between growth zones for *A. punctulata* and *S. franciscanus* (Fig. 5).

On the basis of the aforementioned data, we posited that plate size is determined by relative longitudinal distance from a polar region (apical system or peristome) and column angle (ambulacral or interambulacral). We designed and included in the computational model a function that determines plate size (realised as the diameter for a circle, S_{plate}) in three steps. In the first step, the column type angle (ambulacral or interambulacral) is associated with a plate by calculating its relative latitudinal position within a growth zone. In the second step, Euclidean distance (in the geometric representation) is used to determine in which surface (aboral or oral) a plate is situated, by calculating the longitudinal distance for that plate from the apical system and peristome. In the third step, column angle (α) and distance from the polar region to the plate (d_p) in Eq. (2) are used to calculate S_{plate} . We defined an isosceles triangle, with its vertex at the pole and its two equal-length sides extending from the vertex along a length equal to d_p . The angle opposite to the vertex is equal to α and the length of the base is equal to S_{plate} :

$$S_{plate} = \sqrt{2d_p^2(1 - \cos[\alpha])} \quad (2)$$

We considered plate growth from an integrative perspective; modifications to any region (corona, peristome, or apical system) may result from a change in plate size within that region, and this has ensuing effects on the entire test. For example, if even a single ocular plate were to increase in size, then it would produce an increase in the overall size of the apical system; an increase in the apical system causes a cascade of modifications

throughout the test to maintain relative plate size and column angle relationships.

3.2. Plate addition

Plate addition involves the insertion of new plates at the apical system. Each new plate is situated coterminously with an ocular plate (Jackson, 1912; Gordon, 1926, 1929; Kier, 1956; Mooi et al., 1994). Although numbers and positions for real nucleation points are unknown, previous researchers have utilised the fact that two triangular spaces occur per interambulacrum to simulate interambulacral plate nucleation (e.g., Raup, 1968). We developed the computational model so that each ocular plate could accommodate four nucleation points (two for ambulacral plates and two for flanking interambulacral plates); code functions default to adding one plate per column at each iteration, alternating between nucleation points to mimic plate addition observed in real specimens (Gordon, 1926, 1927, 1929).

We investigated the relationship among the ocular plates, apical system, and ambulacral columns to determine nucleation points and sizes for new plates. We measured ocular plate height (Fig. 1c), ocular plate width (Fig. 1c), and distances from the apical system to ocular plates (d_p in Eq. (2)) to determine nucleation points. We calculated the angles between the outer edges along ocular plates and the apical system centre. Inserting ocular plate size (S_{plate}) and d_p into Eq. (2), we obtained $\alpha = 21 \pm 3^\circ$ and $33 \pm 8^\circ$ for (ambulacra in) *A. punctulata* and *S. franciscanus*, respectively. These angles are similar to the ambulacral column angles

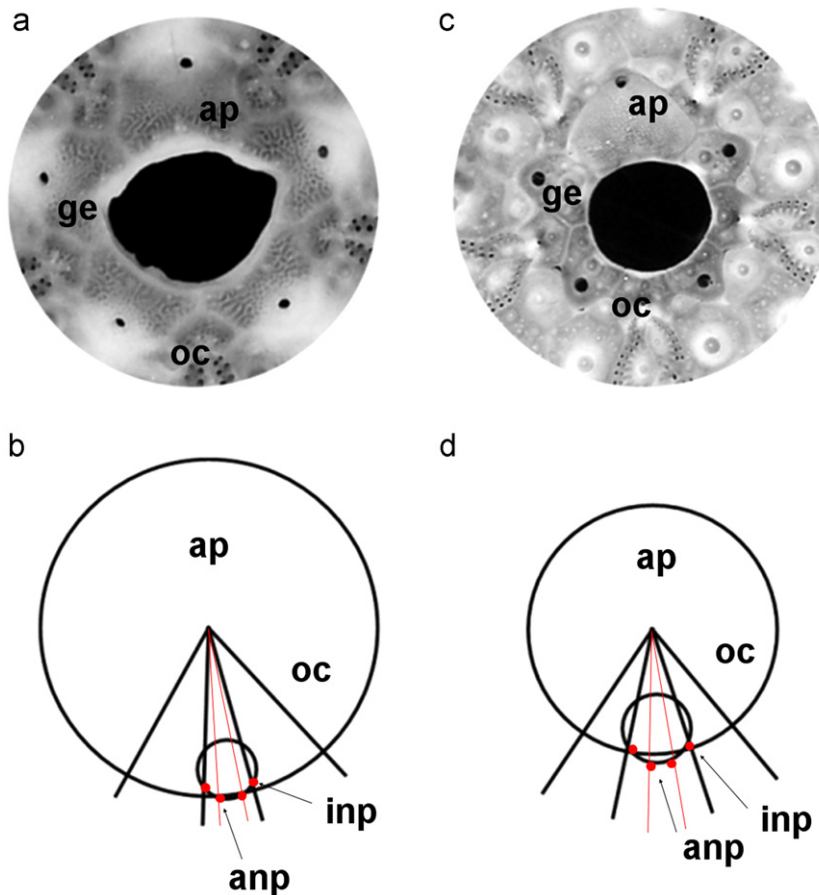


Fig. 6. Sea urchin test morphologies. (a) *A. punctulata* specimen apical system imaged from above. (b) *A. punctulata* apical system represented graphically; the ambulacral column angle ($21 \pm 1^\circ$) delineates ocular plates (thick lines) and nucleation angles (thin lines). (c) *S. franciscanus* specimen apical system imaged from above. (d) *S. franciscanus* apical system represented graphically; the ambulacral column angle ($32 \pm 1^\circ$) delineates ocular plates (thick lines) and nucleation angles (thin lines); apical system (ap), ocular plate (oc), genital plate (ge), interambulacral nucleation points (inp), and ambulacral nucleation points (anp).

previously quantified for the two species ($20 \pm 2^\circ$ and $31 \pm 3^\circ$, respectively; Section 3.1). Based on these empirical data, we conclude that ocular plate size also is determined on the basis of latitudinal position from the apical system (Fig. 6).

Using an ocular plate as a reference, we used the geometric representation and measured the angles associated with new ambulacral plates and new interambulacral plates relative to the apical system, nucleation angles α_{Nam} and α_{Nia} , respectively. The angles $\alpha_{Nam} = 6.96 \pm 1.39^\circ$ and $8.66 \pm 1.87^\circ$ for *A. punctulata* and *S. franciscanus*, respectively; the angles $\alpha_{Nia} = 23.6 \pm 3.76^\circ$ and $34.5 \pm 6.28^\circ$, respectively. We calculated the ratios between ambulacral column angle (α_{am}) and nucleation angles α_{Nam} and α_{Nia} : $\alpha_{Nam}:\alpha_{am} = 0.35:1$ and $0.28:1$ for *A. punctulata* and *S. franciscanus*, respectively; $\alpha_{Nia}:\alpha_{am} = 1.2:1$ and $1.1:1$ for *A. punctulata* and *S. franciscanus*, respectively. On the basis of these values, the angles α_{Nam} and α_{Nia} can be related to the parameter α_{am} , and, thus, we encoded as defaults in the computational model:

$$\alpha_{Nam} = 0.3\alpha_{am}, \quad \alpha_{Nia} = \alpha_{am} \quad (3)$$

The angles α_{Nam} and α_{Nia} allow nucleation points to be located at the periphery along a simulated ocular plate (Fig. 6). Code functions default to inserting nucleation points symmetrically relative to the centre in a simulated ocular plate, two pairs on either side, one for an ambulacral column and one for an interambulacral column.

In real specimens, new ambulacral plates originate underneath ocular plates and interambulacral plates are inserted adjacent to ocular plates (Gordon, 1926; Märkel, 1981). In the computational model, once nucleation points have been determined, new plate sizes are predicted. New ambulacral plate size is calculated using Eqs. (2) and (3). Eq. (2) is used to calculate plate size on the basis of the distance between the nucleation point from the apical system centre (d_p) and the ambulacral nucleation angle (α_{Nam}); α_{Nam} is obtained from Eq. (3).

New interambulacral plate size is calculated by a method that is similar to the aforementioned method for calculating new ambulacral plate sizes (i.e., using Eqs. (2) and (3)), except that, rather than using α_{Nam} , the interambulacral plate angle (α_{Npia}) is used. As α_{Nia} is approximately equal to α_{am} , the computational model determines α_{Npia} as the difference between α_{Nia} and α_{Nam} and dividing by two to obtain a value for one column:

$$\alpha_{Npia} = (\alpha_{Nia} - \alpha_{Nam})/2 \quad (4)$$

3.3. Plate interaction

Plate interaction occurs when plates in a column are in direct contact (even interlocking) with each other (Smith, 1980). We propose that these interactions influence plate shape. As proposed by Raup (1968), advocated by Dafni (1986), and implemented by Abou Chakra and Stone (2008), we used analogy to explain plate interactions. In the analogy, individual plates are likened to bubbles (circles in two dimensions). We modelled plate interactions, implementing Plateau's Laws to predict the interfaces adopted between bubble pairs.

A single bubble adopts a spherical shape because that yields the smallest surface area relative to volume in comparison to other shapes. Similarly, bubbles cluster to minimise the surface area between and among constituent bubbles (Boys, 1958). Plateau's Laws satisfy geometric conditions that are described quantitatively (Isenberg, 1978) by the equations:

$$r_B^{-1} = r_A^{-1} + r_C^{-1} \quad (5)$$

$$|AB|^2 = r_A^2 + r_B^2 + 2r_A r_B \cos[\pi/3] \quad (6)$$

$$|AC|^2 = r_A^2 + r_C^2 + 2r_A r_C \cos[2\pi/3] \quad (7)$$

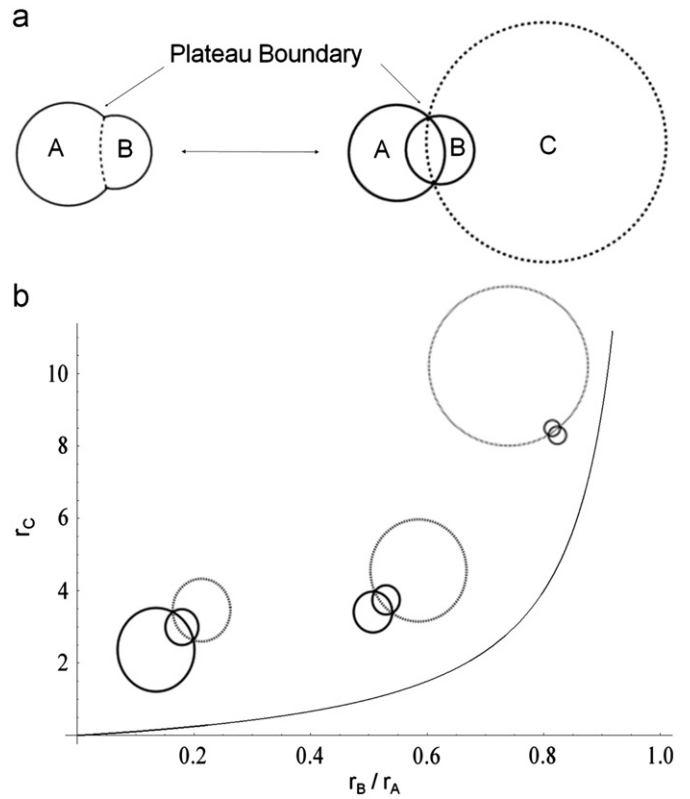


Fig. 7. Plateau boundaries simulated using Eq. (5) to calculate radii for interface boundary circles and pairs of Eqs. (6) and (7) to determine distances between bubbles: (a) unequal-sized bubbles (A and B), yielding a curved interface boundary; (b) a curve showing that the radius for the interface boundary circle C (grey circle) increases as the radius for bubble B (smaller circle) approaches the radius for bubble A (larger circle; the shape of the curve depends on the value of r_a).

These equations quantify the relationships between the curvatures (the inverses of the radii) for a pair of bubbles (A and B) and the curvature for their interface boundary circle (C) (Fig. 7). Eq. (5) is derived from the Young–Laplace equation, in which the pressure differential between the bubbles is calculated by multiplying surface tension by curvature (Young, 1805; Isenberg, 1978); Eq. (5) stipulates that the sum of the curvatures for bubble A and circle C is equal to the curvature for bubble B. Eqs. (6) and (7) use the Cosine Law to calculate, respectively, the distance between the centre for bubble A and the centre for bubble B, given that their radii, r_A and r_B , meet at an angle equal to $\pi/3$ radians, and bubble A and circle C, given that their radii, r_A and r_C , meet at an angle equal to $2\pi/3$ radians (Isenberg, 1978). The three equations are used by the computational model to predict the interface curvature between bubbles, which determines plate shapes and plate patterns.

The interface that is shared by the two bubbles is called a Plateau Boundary (Fig. 7). To determine a Plateau Boundary, two cases are considered, one with equal-sized bubbles and the other with different-sized bubbles. When equal-sized bubbles interact, no pressure differential is produced, and, in accordance with Eq. (5), the radius for circle C (r_C) is infinitely large, so the Plateau boundary is straight (Isenberg, 1978). When unequal-sized bubbles interact, a pressure differential is produced and the smaller bubble B, which contains higher pressure, pushes into the larger bubble A (Isenberg, 1978). The boundary between bubbles is determined by calculating the radius for circle C (r_C), using Eq. (5).

Algorithmically, Eq. (5) generated the radius for an interface boundary circle C (Fig. 7). Then, Eq. (6) yielded the distance between bubble A and bubble B, given their sizes. Lastly, Eq. (7)

returned the distance between bubble A and circle C to determine the position for the Plateau boundary between bubble A and bubble B (Fig. 7).

3.4. Plate gapping

Plate gapping occurs during active growth in regular echinoids, through collagen fibre loosening. Loosening allows plates to separate from one another, creating voids for new plate addition and calcite deposition to occur (Ellers et al., 1998; Johnson et al., 2002). The computational model achieves plate gapping in two dimensions by arranging circles in a close-packing configuration to emulate suture loosening (Fig. 8); theoretically, this is modelled by rearranging circles from their interacting (overlapping) state to a close-packing state, with no overlaps and minimal gaps.

Circle-close-packing arrangements assume a specific tangency pattern, squared or triangular (Fig. 9a and b). The densest circle-close-packing tessellation patterns are triangular, wherein only three circles meet around one point (Aste and Weaire, 2000; Stephenson, 2005). Although equal-sized circle-packing properties are understood and methods are well established (Stephenson, 2005), unequal-sized circle-packing properties (specifically packing without a fixed boundary) are undetermined and methods are lacking. To close-pack circles, we devised and applied an algorithm designed for unequal sized circles. We considered unequal circles because, biologically, plates assume different sizes (Section 3.1).

The computational model arranges unequal-sized circles in a triangular circle-close-packing configuration through three iterative steps. The first step partitions circles into triplets, as determined by a neighbour-finding algorithm that uses proximal distance (measured centre-to-centre); only touching circles are defined as neighbours. The second step arranges the triplets in a close-packing configuration; although triplets comprising unequal sized circles may be arranged in multiple configurations, biologically, plates maintain

relative arrangements. Therefore, the third step involves a 'relative-close-packing' algorithm.

The relative-close-packing algorithm incorporated the Fermat Point, Eq. (8), and Descartes' Circle Theorem, Eq. (9):

$$|\minDist| = |PA| + |PB| + |PC| \quad (8)$$

$$r_D = \frac{r_A r_B r_C (r_B r_C + r_A (r_B + r_C)) \pm 2 \sqrt{r_A} \sqrt{r_B} \sqrt{r_C} \sqrt{r_A + r_B + r_C}}{r_A^2 (r_B - r_C)^2 + r_B^2 r_C^2 - 2 r_A r_B r_C (r_B + r_C)} \quad (9)$$

where the term on the left side in Eq. (8) represents minimum distance; the terms on the right side in Eq. (8) represent the distance between a point, P , and the position for each among three vertices, A , B , and C , in a triangle with sides connecting centres for three tangential circles, A , B , and C , respectively; and r_D in Eq. (9) represents the radius for a circle that occupies the space

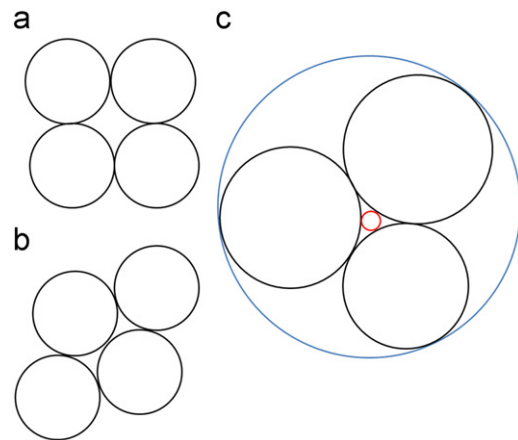


Fig. 9. Circle-close-packing arrangements assume a specific tangency pattern, (a) squared or (b) triangular. Representation for an inner circle (smallest, in centre) and an outer circle (largest, on outside) around a triplet.

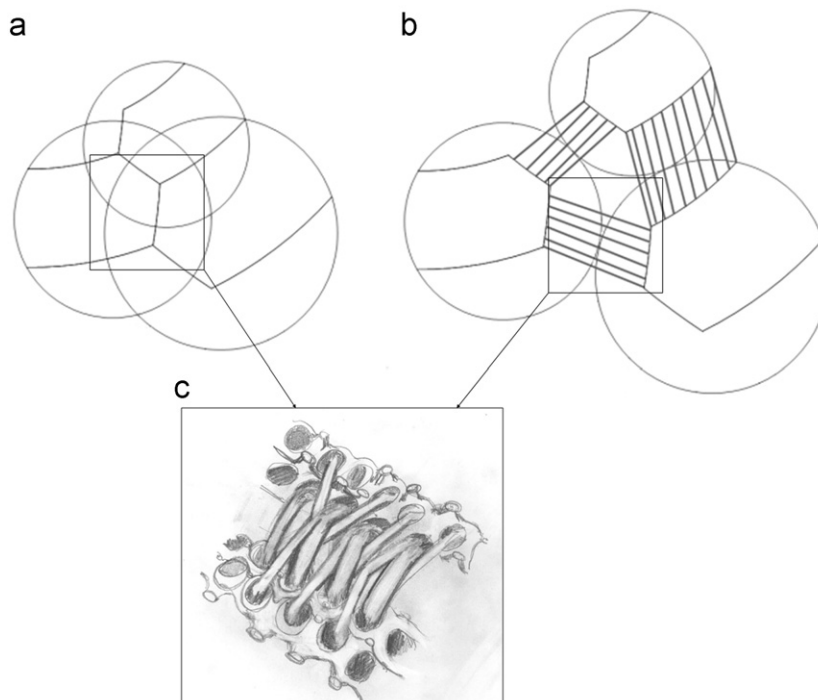


Fig. 8. Plate gapping. (a) Schematic graphic showing three circles in an interacting arrangement and (b) in a close-packing arrangement emulating plate gapping; sutures are displayed linearly for clarity; (c) illustration showing collagen sutures between plates in a real specimen.

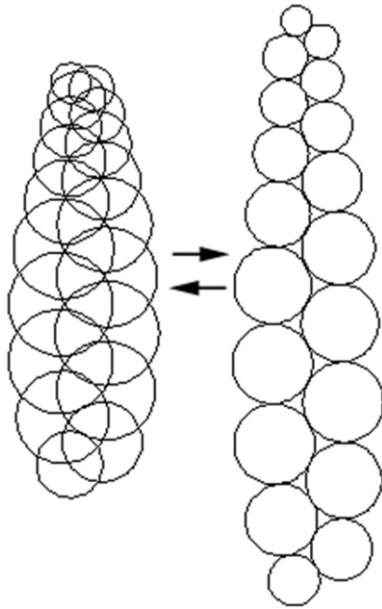


Fig. 10. Animation produced by Holotestoid. An overlapping arrangement for unequal sized circles transformed into a close circle-packing arrangement.

within the three tangential circles, with radii r_A , r_B , and r_C , respectively (Vandeghen, 1964).

The computational model includes a function that determines the centroid amid three circles by calculating the Fermat Point. The Fermat Point marks the location where the summed distances from the centres in the circle triplet is a minimum (Coxeter, 1969). We chose the Fermat Point as the location to initiate close-packing because, within a bubble triplet, it corresponds to the minimum energy point (Lovett and Tilley, 1994). The function uses Descartes' Circle Theorem to determine r_D , the radius for an inner circle (Fig. 9c), which the computational model uses to assign gap sizes. Inner circle radii define the translation required by each circle within a triplet to achieve close-packing. The algorithm yields a triplet, with circles positioned tangentially to each other in a configuration that corresponds to their initial orientation (Fig. 10).

4. Holotestoid: utilising direct, macrostructural ontogenic processes

The four direct, macrostructural ontogenic process are integrated in the computational model Holotestoid. To test Holotestoid, we used it to simulate growth zones and predict values for plate sizes and plate shapes, then compared predicted values to measured values. We also were able to extract additional information, such as interambulacral plate number, interambulacral plate width, and ambitus position.

Holotestoid simulates one growth zone, using the following parameters. Total plate number (tpn) determines how many ambulacral plates will be added throughout a simulation. Growth zone angle (α_{gz}) determines the width for the growth zone being simulated; the default value is 72° . Ambulacral column angle (α_{am}) determines the width for the ambulacral column. Apical system radius (ap_r) defines the size for the apical system. Peristome radius to apical system radius ratio ($ps_r:ap_r$) provides a constant relative size relation for the test. Apical system radius to column length ratio ($ap_r:cl$) provides the computational model with another constant relative size relation ($ap_r:cl=0$ constitutes a special case, which Holotestoid translates to no growth for the polar regions).

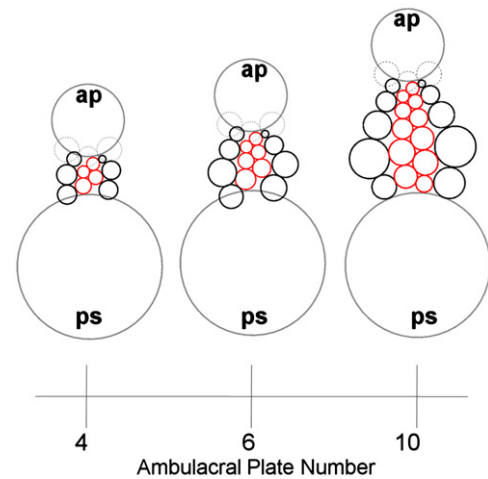


Fig. 11. Schematic graphic showing interambulacral plates (black, outer circles) arranged around ambulacral columns (light, inner circles), with apical system (ap , grey circle), peristome (ps , grey circle), ocular plates (dashed circle in the centre), and two flanking genital plates (dashed circles). The computational model inserts interambulacral plates with respect to the ambulacral column length. As ambulacral plate number increased, interambulacral plate number also increased.

The computational model is designed to allow plates to be added exclusively to one column type (ambulacral, for instance); it thereby provides a tool for predicting morphological variables, such as interambulacral plate number, interambulacral plate width, and ambitus position. Interambulacral plates may influence test shape (Märkel, 1981), and interambulacral plate numbers and interambulacral plate sizes vary among species (Kier, 1974). To accommodate their effects computationally, we designed and included in the computational model a function that predicts how many interambulacral plates are required to surround a simulated ambulacral column (Fig. 11). Using that function, the computational model continuously adds interambulacral plates adjacent to ocular plates until the column spanning from the apical system to the peristome is packed. As an ambulacral column increases in length, interambulacral plates increase in size (Fig. 11).

We performed two different simulations. First, we varied the ambulacral column angle (α_{am}) exclusively (*i.e.*, all other parameters fixed) to investigate its influence on growth zone shape. Second, we varied α_{am} , peristome radius to apical system radius ratio ($ps_r:ap_r$), and apical system radius to column length ratio ($ap_r:cl$) (*i.e.*, all other parameters fixed) to test the analogies used for plate interaction and plate gapping.

4.1. Growth zones α_{am}

We hypothesised that ambulacral column angle is a crucial parameter to differentiate growth zones among species. We simulated two growth zones, one for *A. punctulata* and another for *S. franciscanus*, by varying the α_{am} ($\alpha_{am}=20^\circ$ for *A. punctulata* and $\alpha_{am}=31^\circ$ for *S. franciscanus*; the other parameters were fixed at $tpn=40$, $\alpha_{gz}=72^\circ$, $ap_r=0.05$ mm, $ps_r:ap_r=1$, and $ap_r:cl=0$).

Using the emulated plate interaction process, we mimicked plate boundaries in a column (Fig. 12). The computational model arranged plates in an overlapping configuration, and the boundaries between them were determined using the function that describes the plate interaction process. Qualitatively, the growth zone for *A. punctulata* ($\alpha_{am}=20^\circ$) was narrower than the growth zone for *S. franciscanus* ($\alpha_{am}=31^\circ$, Fig. 12). Plate widths between the two growth zones differed, being larger in *S. franciscanus* (Fig. 12).

To assess growth results from these simulations, we utilised the fact that the computational model inserts interambulacral

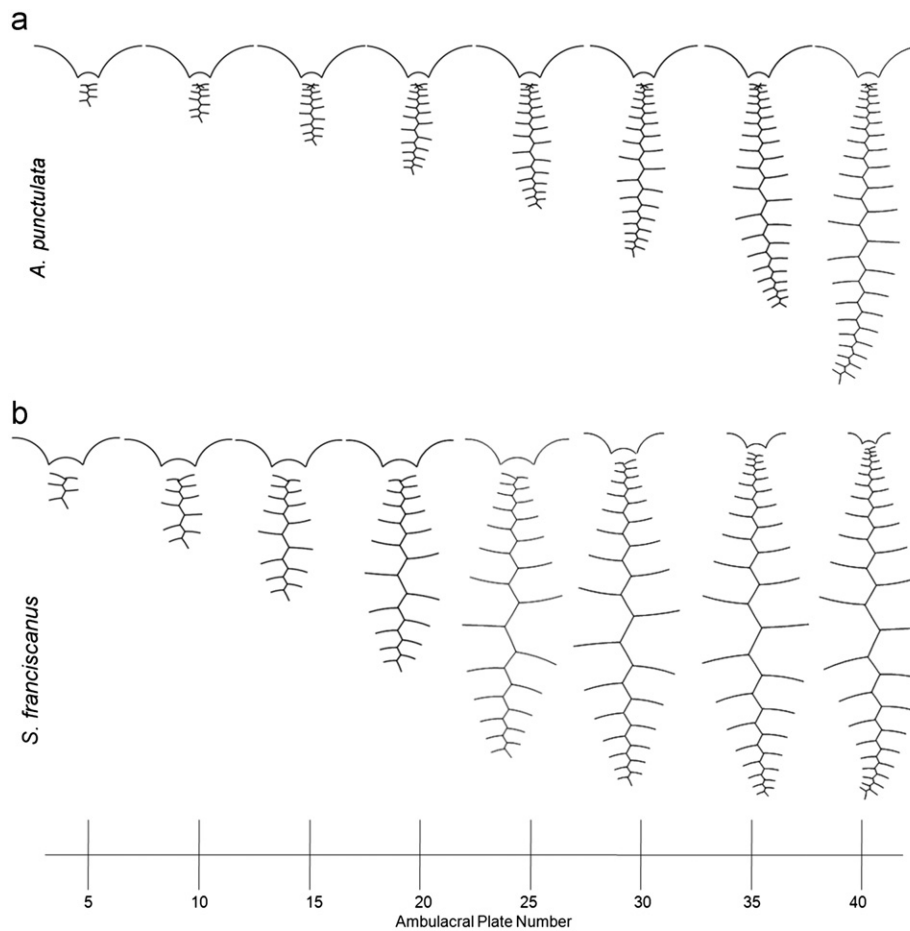


Fig. 12. Two growth zones, one for *A. punctulata* and another for *S. franciscanus*, simulated by changing the parameter α_{am} ($\alpha_{am}=20^\circ$ for *A. punctulata* and $\alpha_{am}=31^\circ$ for *S. franciscanus*; other parameters fixed: $tpn=40$, $\alpha_{gz}=72^\circ$, $ap_r=0.05$ mm, and $ps_r:ap_r=1$).

plates around ambulacral columns and compared values from simulated specimens to data that were obtained from real specimens. We plotted (plate number, plate width) pairs for interambulacral columns (Fig. 5). In the computational model, plates are represented as circles, and, thus, comparisons were limited to plate widths (i.e., circle diameters). Additionally, simulations were conducted under the condition that the apical system and peristome retained constant sizes, and, thus, comparisons were limited to qualitative observations, from which correspondence was apparent (cf. Fig. 5b, c, e and f). For instance, interambulacral plate width increased with increasing plate number (Fig. 5b, c, e and f).

We also obtained interambulacral-to-ambulacral plate ($ia:am$) ratios from simulations. We included in our calculations ambulacral plate compounding (as real ambulacral plates are fused composites), whereby three plates were combined to create each ambulacral plate for *A. punctulata* and five plates were combined to create each ambulacral plate for *S. franciscanus* (Gordon, 1929; Kier, 1974). Simulations for *A. punctulata* yielded $ia:am=0.21$ and simulations for *S. franciscanus* yielded $ia:am=0.18$; published ratios (Kier, 1974) are 0.22 for *A. punctulata* and 0.12 for *S. franciscanus*.

We also used the computational model to predict ambitus position. We hypothesised *a priori* that the ambitus was located half way along a growth zone (i.e., equidistant, as measured from the polar region centres) and set that as an initial condition for simulations. Plate width increased with increasing distance from either pole, reaching a maximum at the ambitus. Maximum measured plate width for *A. punctulata* occurred at a distance between 62% and 68% from the apical system centre (Fig. 13a) and maximum predicted plate width occurred at a distance between

47% and 61% (Fig. 13b). Maximum measured plate width for *S. franciscanus* occurred at a distance between 55% and 65% from the apical system centre (Fig. 13c) and maximum predicted plate width occurred at a distance between 48% and 59% (Fig. 13d). Although we set the initial condition for the ambitus to be exactly equidistant from either pole (i.e., at a distance exactly 50% from the apical system), through emulated growth processes, the ambitus position deviated to different locations in simulations.

4.2. Growth zones α_{am} - $ps_r:ap_r$ - $ap_r:cl$

We expanded our analysis to test the analogies used for plate interaction and plate gapping. We simulated four growth zones, one each for *E. thoursii* (Cidaroida), *A. punctulata*, *S. franciscanus*, and *M. quinquesperforata* (Clypeasteroida) because they exhibit diverse test morphologies (from tall-globose in *E. thoursii*, to flat-discoid in *M. quinquesperforata*). For these simulations, three parameters were fixed: $tpn=40$, $\alpha_{gz}=72^\circ$, and $ap_r=0.05$ mm. For *E. thoursii*, we used $\alpha_{am}=16^\circ$, $ps_r:ap_r=1.33$, and $ap_r:cl=0.18$. For *A. punctulata*, we used $\alpha_{am}=20^\circ$, $ps_r:ap_r=1.97$, and $ap_r:cl=0.14$. For *S. franciscanus*, we used $\alpha_{am}=32^\circ$, $ps_r:ap_r=2.5$, and $ap_r:cl=0.09$. For *M. quinquesperforata*, we used $\alpha_{am}=39^\circ$, $ps_r:ap_r=0.53$, and $ap_r:cl=0.04$. All values used were obtained from measured data that we acquired from real specimens.

Simulated growth zones (Fig. 14) resembled growth zones in real specimens. Plate gaps were simulated for *E. thoursii*, *A. punctulata*, *S. franciscanus*, and *M. quinquesperforata* (Fig. 14a–d, respectively—with plates represented by close-packed circles). Plate interactions, where circles overlapped according to the bubble

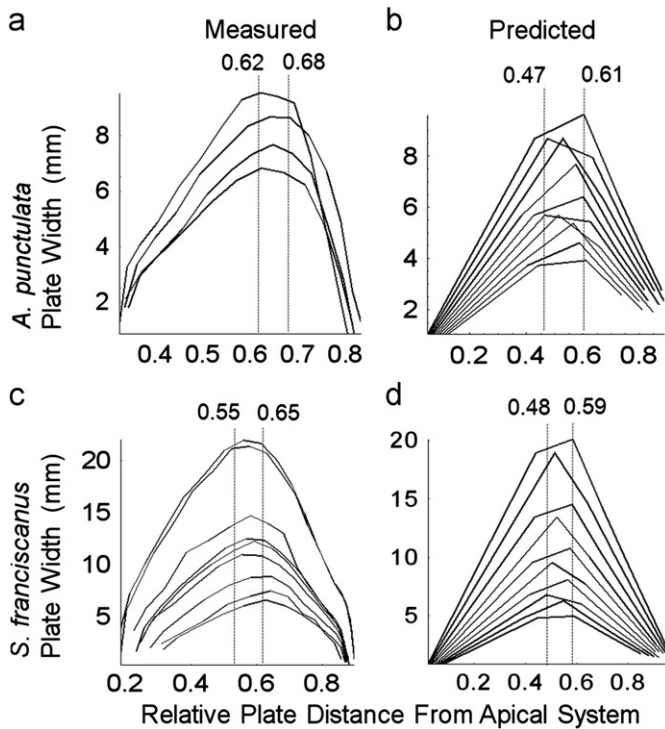


Fig. 13. Measured and predicted plate width values plotted against relative distance from the apical system for an interambulacral column (as a proportion). Columns are depicted on the basis of total plate number, shown as a single curve in the plot. *A. punctulata* (a) measured plate width values from specimens containing 12–15 *ia* plates, with maximum plate width occurring at a distance between 62% and 68% of growth zone length; (b) predicted plate width values from simulation producing specimen containing 8–12 *ia* plates, with maximum plate width occurring at a distance between 47% and 61% along growth zone length. *S. franciscanus* (c) measured plate width values from specimens containing 12–20 *ia* plates, with maximum plate width occurring at a distance between 55% and 65% along growth zone length; (d) predicted plate width values from simulation producing specimen containing 12–18 *ia* plates, with maximum plate width occurring at a distance between 48% and 59% along growth zone length.

analogy, yielded realistic plate shapes and plate boundary curvatures (Fig. 14). Each growth zone is associated with an apical system (top) and a peristome (bottom) at either polar region. The sizes for these regions are determined by $ps_r:ap_r$ and $ap_r:cl$.

4.3. Limitations

The computational model is limited in at least six aspects. First, plates are analogised as bubbles and are represented as circles, so only plate widths could be compared between simulated and real specimens (Sections 3 and 4); the bubble analogy and geometric representation are used in a purely geometric sense to simulate morphological patterns produced by emulated growth processes (*i.e.*, surface tension might play no role in echinoid growth; Raup, 1968). Second, in the computational model, new plates may be added in quartets (*i.e.*, with each ocular plate accommodating two nucleation points for ambulacral plates and two nucleation points for flanking interambulacral plates, alternating for each plate addition step; Section 3.2) or in pairs (*i.e.*, exclusively to one column type, such as ambulacral, whereupon interambulacral plates are added to populate interambulacral columns; Section 4.1); in real specimens, locations and numbers for new plate nucleation points are unknown and new plates are added at different rates throughout development (Gordon, 1926; Raup, 1968; Smith, 1984). Third, in the computational model, a single growth zone is simulated (Section 4.1); in real specimens, 5 growth zones develop simultaneously and typically differ from one another. Fourth, biserial column morphologies are

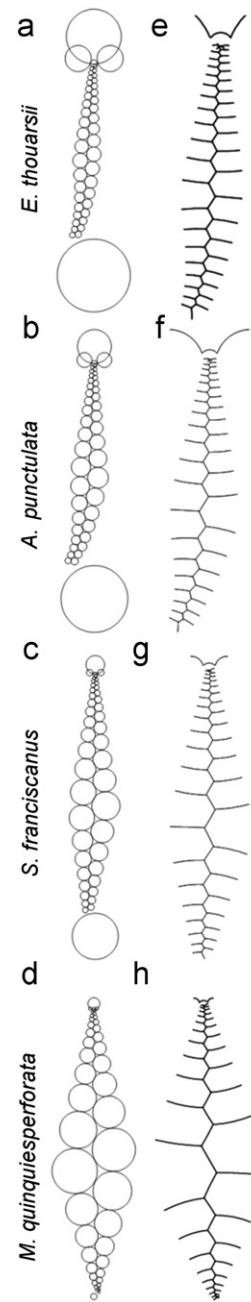


Fig. 14. Simulated growth zones for *E. Thouarsii*, *A. punctulata*, *S. franciscanus*, and *M. quinquiesperforata* (parameter values are listed in the text). Plate gapping is shown in (a–d). Plate interaction is shown in (e–g).

produced (four columns constituting a growth zone); among real specimens, this would accommodate only some echinoid test morphologies—most Palaeozoic echinoid tests have more than four columns in a growth zone (Smith, 2005). Fifth, the computational model simulates circles representing bubbles, which are added together in enumerating plates; real ambulacral plates in extant echinoids are fused composites. Sixth, echinoid tests comprise 5 growth zones, associated in three dimensions; the computational model involves two-dimensional projections.

5. Conclusion

Growth zones for *A. punctulata* and for *S. franciscanus* were generated by varying only a single parameter, the ambulacral

column angle ($\alpha_{am}=22^\circ$ and $\alpha_{am}=32^\circ$, respectively; Section 4.1). Therefore, ambulacral column angle is a parameter that can distinguish species; herein, it determined different plate sizes and, therefore, different simulated morphologies, representing two species. Changes in plate size, even to a single plate, stimulates changes in surrounding regions. We showed that ocular plate size is influenced by ambulacral column angle, which then influences the position and size for new plates added to the corona (Sections 3 and 4).

In the computational model, any shift in plate location stimulated a change (increase or decrease) in plate size. Simulations produced plate patterns corroborating observed trends (e.g., plate size increases with increasing distance from polar regions, maximising at the ambitus; Section 3.1). More importantly, using one parameter, we were able to simulate test morphologies mimicking patterns produced by growth processes for two different species (Sections 3 and 4).

A prospective direction for additional development with Holotestoid involves including the indirect macrostructural ontogenic process visceral growth. Visceral growth involves the integrated effects imparted by somatic growth onto skeletal structures (Deutler, 1926; Gordon, 1926, 1927, 1929; Hyman, 1955; Moss and Meehan, 1968; Eilers and Telford, 1992). Previous models that included visceral growth qualitatively described echinoid test shapes (e.g., Thompson, 1917; Moss and Meehan, 1968; Seilacher, 1979; Baron, 1990, 1991; Eilers, 1993; Zachos, 2009). In some cases, mathematical relations were utilised to associate with visceral growth mathematical curves that describe test outlines. For example, the Young–Laplace equation was considered previously by Thompson (1917), in the liquid drop model, and Eilers (1993), in the membrane model (the membrane model was found to be limited in its application, simulating inaccurately test outlines characterising Cidaroida and Irregularia).

Holotestoid is designed to implement any mathematical function to represent visceral growth (e.g., parabolic or hyperbolic). Catenary chains constitute one function that we have explored (Abou Chakra, 2010). Catenaries describe the shapes that would be assumed by an inextensible but flexible chain that hangs freely from two fixed points at equal heights (Bernoulli, 1691; Huygens, 1691; Leibniz, 1691; Yates, 1959) and have been associated with natural growth and form patterns, such as tree trunks, dental arches, and spider-webs (Witt and Reed, 1965; BeGole, 1981; Harker, 1996). As is the case with applying any function, suitable justifications, empirical and biological, are requisite before catenaries may be included formally in Holotestoid.

The ability to simulate different species is useful especially for echinoids because they exhibit a rich fossil history, and some fossil species descriptions are based on a single incomplete specimen (Kier, 1977; Smith, 2005). For such incomplete specimens, Holotestoid becomes useful because researchers can make inferences about test growth, using only a few measurements to estimate parameters and run simulations (i.e., to reconstruct graphically entire specimens). We are confident that Holotestoid is a useful tool for describing and explaining the evolutionary-developmental changes and morphological disparity that are observed among echinoid tests.

Acknowledgements

We would like to thank our reviewers for their insightful comments and intellectual input from A. Ahuja, A. Dey, B. Evans, B. Golding, M. Lovric, R. Mooi, K.R. Moonosawmy, and R. Morton. Illustrations were created, digital images were captured, and source code was written by M. Abou Chakra. Support was provided through the Shared Hierarchical Academic Research Computing Network. Funding was provided by the Department

of Biology at McMaster University, Ontario Ministry of Training, Colleges, and Natural Sciences and Engineering Research Council of Canada (Discovery Grant 261590).

Appendix A. Supplementary material

Supplementary data associated with this article can be found in the online version at doi:10.1016/j.jtbi.2011.06.019.

References

- Abou Chakra, M., 2010. Modelling Echinoid Skeletal Growth and Form. Ph.D. Thesis. McMaster University.
- Abou Chakra, M., Stone, J.R., 2008. Descartes, Plateau, and sea urchins. In: Brebbia, C.A. (Ed.), WIT Transactions on Ecology and the Environment. WIT Press, pp. 97–105.
- Abou Chakra, M., Stone, J.R., 2011. Classifying echinoid skeleton models: testing ideas about growth and form. *Paleobiology* 37 (4), 686–695.
- Aste, T., Weaire, D.L., 2000. *The Pursuit of Perfect Packing*. Institute of Physics Publication, Bristol, Philadelphia, PA.
- Baron, C.J., 1990. What functional morphology cannot explain: a model of sea urchin growth and a discussion of the role of morphogenetic explanations in evolutionary biology. In: Dudley, E.C. (Ed.), *The Unity of Evolutionary Biology* (Proceedings of the Fourth International Congress of Systematic and Evolutionary Biology). Dioscorides Press, Portland, Oregon, pp. 471–488.
- Baron, C.J., 1991. The Structural Mechanics and Morphogenesis of Extant Regular Echinoids Having Rigid Tests. Ph.D. Thesis. University of California at Berkeley.
- BeGole, E.A., 1981. A computer program for the analysis of dental arch form using the catenary curve. *Computer Programs in Biomedicine* 13, 93–99.
- Bernoulli, J., 1691. *Solutio problematis funicularii*. *Acta Eruditorum*, 274–276.
- Boys, S.C.V., 1958. *Soap Bubbles their Colors and Forces which Mold Them*. Doubleday Anchor Books, Garden City, NY.
- Coxeter, H.S.M., 1969. *Introduction To Geometry*. Wiley, New York.
- Dafni, J., 1986. A biomechanical model for the morphogenesis of regular echinoid tests. *Paleobiology* 12, 143–160.
- Deutler, F., 1926. Über das Wachstum des Seeigelskeletts. *Zoologische Jahrbücher. Abteilung für Anatomie und Ontogenie der Tiere* 48, 119–200.
- Ebert, T.A., Southon, J.R., 2003. Red sea urchins (*Strongylocentrotus franciscanus*) can live over 100 years: confirmation with A-bomb (14) carbon. *Fishery Bulletin* 101, 915–922.
- Eilers, O., 1993. A mechanical model of growth in regular sea urchins: predictions of shape and a developmental morphospace. *Proceedings of the Royal Society of London Series B—Biological Sciences* 254, 123–129.
- Eilers, O., Telford, M., 1992. Causes and consequences of fluctuating coelomic pressure in sea urchins. *Biological Bulletin* 182, 424–434.
- Eilers, O., Johnson, A.S., Moberg, P.E., 1998. Structural strengthening of urchin skeletons by collagenous sutural ligaments. *Biological Bulletin* 195, 136–144.
- Gordon, I., 1926. The development of the calcareous test of *Echinus miliaris*. *Philosophical Transactions of the Royal Society of London, Series B, Containing Papers of Biological Character* 214, 259–312.
- Gordon, I., 1927. The development of the calcareous test of *Echinocardium cordatum*. *Philosophical Transactions of the Royal Society of London, Series B, Containing Papers of Biological Character* 215, 255–313.
- Gordon, I., 1929. Skeletal development in Arbacia, Echinarachnius, and Leptasterias. *Philosophical Transactions of the Royal Society of London, Series B, Containing Papers of Biological Character* 217, 289–334.
- Harker, R.I., 1996. Curved tree trunks: indicators of soil creep and other phenomena. *The Journal of Geology* 104, 351–358.
- Huygens, C., 1691. *Dynaste Zulichemii, solutio problematis funicularii*. *Acta Eruditorum*, 281–282.
- Hyman, L.H., 1955. *The Invertebrates: Echinodermata*. McGraw-Hill Book Company, New York.
- Isenberg, C., 1978. *The Science of Soap Films and Soap Bubbles*. Tieto Ltd., England.
- Jackson, R.T., 1912. Phylogeny of the Echini, with a revision of Palaeozoic species. *Boston Society of Natural History, Memoirs*, 1–490.
- Johnson, A.S., Eilers, O., Lemire, J., Minor, M., Leddy, H.A., 2002. Sutural loosening and skeletal flexibility during growth: determination of drop-like shapes in sea urchins. *Proceedings of the Royal Society of London, Series B—Biological Sciences* 269, 215–220.
- Kier, P.M., 1956. Separation of interambulacral columns from the apical system in the Echinoidea. *Journal of Paleontology* 30, 971–974.
- Kier, P.M., 1974. Evolutionary trends and their functional significance in the post-Palaeozoic echinoids. *Memoir (The Paleontological Society)* 5, 1–95.
- Kier, P.M., 1977. The poor fossil record of the regular echinoid. *Paleobiology* 3, 168–174.
- Leibniz, G., 1691. *Solutio problematica catenarii*. *Acta Eruditorum*, 277–281.
- Lovett, D.R., Tilley, J., 1994. *Demonstrating Science with Soap Films*. Institute of Physics Publishing, Bristol, Philadelphia.
- Märkel, K., 1981. Experimental morphology of coronar growth in regular echinoids. *Zoomorphology* 97, 31–52.

- Märkel, K., Roser, U., 1983. Calcite-resorption in the spine of the echinoid *Eucidaris tribuloides*. *Zoomorphology* 103, 43–58.
- Märkel, K., Roser, U., 1985. Comparative morphology of echinoderm calcified tissues—histology and ultrastructure of ophiuroid scales (Echinodermata, Ophiuroidea). *Zoomorphology* 105, 197–207.
- Mooi, R., David, B., 1996. Embryology supports a new theory of skeletal homologies for the phylum Echinodermata. *Comptes Rendus de l'Académie des Sciences* 319, 577–584.
- Mooi, R., David, B., Marchand, D., 1994. Echinoderm skeletal homologies: classical morphology meets modern phylogenetics. In: David, B., et al. (Eds.), *Echinoderms through Time: Proceedings of the Eighth International Echinoderm Conference*, Dijon, France, pp. 87–95.
- Moss, M.L., Meehan, M., 1967. Structural connective tissues in the test of the echinoid *Arbacia punctulata*. *Acta Anatomica* 66, 279–304.
- Moss, M.L., Meehan, M., 1968. Growth of the echinoid test. *Acta Anatomica* 69, 409–444.
- Pearse, J.S., Pearse, V.B., 1975. Growth zones in the echinoid skeleton. *American Zoologist* 15, 731–753.
- Raup, D.M., 1968. Theoretical morphology of echinoid growth. *Journal of Paleontology* 42, 50–63.
- Seilacher, A., 1979. Constructional morphology of sand dollars. *Paleobiology* 5, 191–221.
- Smith, A.B., 1980. Stereom Microstructure of the Echinoid Test. *Palaeontological Association*, London.
- Smith, A.B., 1984. *Echinoid Palaeobiology*. Allen & Unwin, London.
- Smith, A.B., 2005. Growth and form in Echinoids: the evolutionary interplay of plate accretion and plate addition. In: Briggs, D.E.G., Seilacher, A. (Eds.), *Evolving Form and Function: Fossils and Development*. Yale Peabody Museum Publications, New Haven, Connecticut, pp. 181–195.
- Stephenson, K., 2005. *Introduction to Circle Packing: The Theory of Discrete Analytic Functions*. Cambridge University Press, Cambridge, UK, New York.
- Telford, M., 1985. Domes, arches and urchins: the skeletal architecture of echinoids (Echinodermata). *Zoomorphology* 105, 114–124.
- Telford, M. (Ed.), 1994. *Structural Models and Graphical Simulation of Echinoids*. Balkema, Rotterdam.
- Thompson, D.A.W., 1917. *On Growth and Form*. Press Syndicate of the University of Cambridge, Cambridge, UK.
- Vandeghen, A., 1964. Soddy's Circles and the De Longchamps point of a triangle. *The American Mathematical Monthly* 71, 176–179.
- Vermeij, G.J., 1970. Adaptive versatility and skeleton construction. *American Naturalist* 104, 253–260.
- Witt, P.N., Reed, C.F., 1965. Spider-web building. *Science* 149, 1190–1197.
- Yates, R.C., 1959. The catenary and the tractrix. *The American Mathematical Monthly* 66, 500–505.
- Young, T., 1805. An essay on the cohesion of fluids. *Philosophical Transactions of the Royal Society of London* 95, 65–87.
- Zachos, L.G., 2009. A new computational growth model for sea urchin skeletons. *Journal of Theoretical Biology* 259, 646–657. doi:10.1016/j.jtbi.2009.04.007.